

UC Santa Barbara

UC Santa Barbara Previously Published Works

Title

Measles Virus Forms Inclusion Bodies with Properties of Liquid Organelles

Permalink

<https://escholarship.org/uc/item/24q3615j>

Journal

Journal of Virology, 93(21)

ISSN

0022-538X

Authors

Zhou, Yuqin

Su, Justin M

Samuel, Charles E

et al.

Publication Date

2019-11-01

DOI

10.1128/jvi.00948-19

Peer reviewed



Measles Virus Forms Inclusion Bodies with Properties of Liquid Organelles

Yuqin Zhou,^{a*} Justin M. Su,^a Charles E. Samuel,^a Dzwokai Ma^a

^aDepartment of Molecular, Cellular and Developmental Biology, University of California, Santa Barbara, California, USA

ABSTRACT Nonsegmented negative-strand RNA viruses, including measles virus (MeV), a member of the *Paramyxoviridae* family, are assumed to replicate in cytoplasmic inclusion bodies. These cytoplasmic viral factories are not membrane bound, and they serve to concentrate the viral RNA replication machinery. Although inclusion bodies are a prominent feature in MeV-infected cells, their biogenesis and regulation are not well understood. Here, we show that infection with MeV triggers inclusion body formation via liquid-liquid phase separation (LLPS), a process underlying the formation of membraneless organelles. We find that the viral nucleoprotein (N) and phosphoprotein (P) are sufficient to trigger MeV phase separation, with the C-terminal domains of the viral N and P proteins playing a critical role in the phase transition. We provide evidence suggesting that the phosphorylation of P and dynein-mediated transport facilitate the growth of these organelles, implying that they may have key regulatory roles in the biophysical assembly process. In addition, our findings support the notion that these inclusions change from liquid to gel-like structures as a function of time after infection, leaving open the intriguing possibility that the dynamics of these organelles can be tuned during infection to optimally suit the changing needs during the viral replication cycle. Our study provides novel insight into the process of formation of viral inclusion factories, and taken together with earlier studies, suggests that *Mononegavirales* have broadly evolved to utilize LLPS as a common strategy to assemble cytoplasmic replication factories in infected cells.

IMPORTANCE Measles virus remains a pathogen of significant global concern. Despite an effective vaccine, outbreaks continue to occur, and globally ~100,000 measles-related deaths are seen annually. Understanding the molecular basis of virus-host interactions that impact the efficiency of virus replication is essential for the further development of prophylactic and therapeutic strategies. Measles virus replication occurs in the cytoplasm in association with discrete bodies, though little is known of the nature of the inclusion body structures. We recently established that the cellular protein WD repeat-containing protein 5 (WDR5) enhances MeV growth and is enriched in cytoplasmic viral inclusion bodies that include viral proteins responsible for RNA replication. Here, we show that MeV N and P proteins are sufficient to trigger the formation of WDR5-containing inclusion bodies, that these structures display properties characteristic of phase-separated liquid organelles, and that P phosphorylation together with the host dynein motor affect the efficiency of the liquid-liquid phase separation process.

KEYWORDS WD repeat-containing protein WDR5, inclusion body, innate immunity, liquid-liquid phase separation, measles virus

The *Mononegavirales* possess linear single-stranded RNA (ssRNA) genomes of negative polarity (1, 2). Some of these viruses are significant human pathogens, including measles virus (MeV), Nipah virus (NiV), parainfluenza viruses (PIVs), mumps virus

Citation Zhou Y, Su JM, Samuel CE, Ma D. 2019. Measles virus forms inclusion bodies with properties of liquid organelles. *J Virol* 93:e00948-19. <https://doi.org/10.1128/JVI.00948-19>.

Editor Rebecca Ellis Dutch, University of Kentucky College of Medicine

Copyright © 2019 American Society for Microbiology. All Rights Reserved.

Address correspondence to Charles E. Samuel, samuel@lifesci.ucsb.edu, or Dzwokai Ma, dzwokai.ma@lifesci.ucsb.edu.

* Present address: Yuqin Zhou, Isotope Research Laboratory, Department of Biological Engineering and Application Biology, Sichuan Agricultural University, Ya'an, People's Republic of China.

Received 6 June 2019

Accepted 26 July 2019

Accepted manuscript posted online 2 August 2019

Published 15 October 2019

(MuV), respiratory syncytial virus (RSV), metapneumovirus (HMPV), rabies virus (RABV), and Ebola virus (EBOV). Among them, MeV (a member of the *Paramyxoviridae* family) is highly contagious and still represents a major global health risk. In the United States, increasing numbers of cases and outbreaks of measles have been reported during recent years after the disease was declared eradicated in 2000 (3).

During viral entry, the MeV virion envelope fuses with the host cell membrane, thereby leading to the release of the RNA nucleocapsid into the cytoplasm of the infected cell. The ~15.9-kb negative-strand ssRNA genome is encapsidated by the nucleoprotein (N), which in turn is associated with the viral RNA polymerase complex consisting of the large (L) and phospho- (P) viral proteins (1, 4). The association between the nucleocapsid and the polymerase is achieved via the binding between the molecular recognition element (MoRE) of N and the XD domain of P (5, 6). Together, these viral proteins (N, P, and L) and the RNA genome form a ribonucleoprotein (RNP) complex that constitutes the basic machinery responsible for transcription and then replication (7, 8). The matrix (M) protein mediates the assembly of progeny enveloped virions that possess two viral glycoproteins, the hemagglutinin (H) and fusion (F) proteins (9). In addition to the above-mentioned structural proteins, the MeV P gene also encodes two nonstructural accessory proteins, V (10) and C (11), important for modulating host innate responses to infection (12, 13).

Transcription and replication of MeV RNPs are thought to take place in specific cytoplasmic factories called inclusion bodies (IBs) (14–16). IBs are membraneless compartments (17) enriched with N, P, and L proteins (16, 18). Similar IB structures are observed in the cells infected by MuV (19), NiV (20), PIV3 (21), and PIV5 (22), four additional members of the *Paramyxoviridae* family; RSV (23) and HMPV (24), two members of the *Pneumoviridae* family; RABV (25) and vesicular stomatitis virus (VSV) (26), two members of the *Rhabdoviridae* family; and EBOV (27), a member of the *Filoviridae* family. Although IBs are believed to represent major sites of viral transcription and replication of *Mononegavirales*, how IBs are formed and regulated is little understood. Even though we and others have identified host proteins localized to IBs (28–30), including the WD repeat-containing protein 5 (WDR5) (16), the identity and function of IB-associated host factors largely remain unknown. A technical hurdle is that the isolation and purification of IBs have proven challenging, partially due to the lack of a membrane separating IBs from other cytoplasmic constituents. Elucidation of the mechanisms by which IBs are assembled and regulated is key to understanding how IBs promote viral multiplication.

By labeling IBs using mCherry or enhanced green fluorescent protein (EGFP) fusions of the P protein from RABV (31) and VSV (32), two recent reports proposed that IB assembly triggered by infection with these related viruses is mediated via liquid-liquid phase separation (LLPS), a process described for the formation of other subcellular membraneless organelles (33–37). Whereas these studies provide important insight into the biogenesis of IBs by members of the *Rhabdoviridae* family (31, 32), whether LLPS drives IB formation with other negative-strand RNA viruses has yet to be demonstrated. It is also unclear whether any regulatory mechanisms exist to control IB assembly. Here, we show that measles virus triggers the formation of IBs that are assembled by LLPS, thereby extending LLPS findings from *Rhabdoviridae* to *Paramyxoviridae*. In addition, we identified domain regions of the MeV N and P proteins that are essential for this LLPS process, and we showed that the phosphorylation of MeV P and the dynein-dependent transport system represent two mechanisms that affect the size and spatial distribution of IBs within MeV-infected cells. Finally, we provide evidence consistent with the notion that IB maturation facilitates MeV replication. Thus, our study not only further establishes LLPS as a common process to mediate IB formation across the *Mononegavirales* but also sheds new insights into the biogenesis, regulation, and function of viral inclusion bodies.

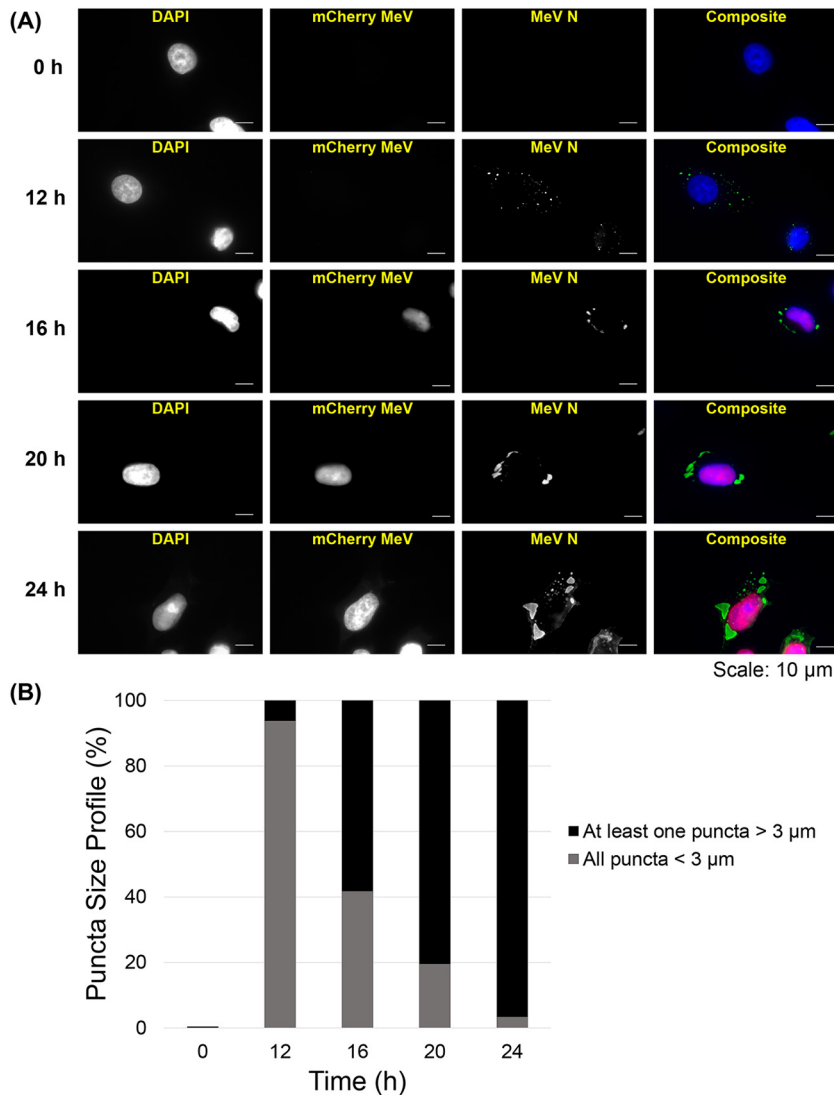


FIG 1 Time course of changes in viral inclusion body formation following measles virus infection. HeLa cells were infected (MOI, 5) with recombinant measles virus (MeV vac2) isogenic to the Moraten vaccine strain engineered to express mCherry protein with a nuclear localization signal. Cells were fixed with formaldehyde at the indicated time after infection, immunostained for MeV N protein or stained with DAPI for DNA, and subjected to fluorescent imaging analysis. (A) Representative images at each time point after infection. Scale bars = 10 μm. (B) Quantitation of time course analysis of inclusion body size, based on the longest path from two ends of the largest puncta in each cell. Black, at least one punctum larger than 3 μm; gray, all puncta less than 3 μm. A total of 500 cells were examined.

RESULTS

Cytoplasmic inclusion bodies induced by measles virus infection display increased size and altered morphology in a time-dependent manner. When HeLa cells infected by MeV were examined by fluorescent imaging at 24 h postinfection (pi), the induced IB-containing viral replication proteins displayed a mixed pattern of sizes and shapes. These ranged from small spherical cytoplasmic puncta to larger structures of irregular shapes (16). To test whether a relationship exists between the size and shape heterogeneity of IBs and the duration of infection, we carried out a time course study at a high multiplicity of infection (MOI, 5). Recombinant virus isogenic to the Moraten vaccine strain was used that expressed mCherry possessing a nuclear localization signal. Imaging analyses were carried out at increasing times postinfection after fixing and staining with anti-N antibody and 4',6-diamidino-2-phenylindole (DAPI) (Fig. 1A). In 95% of the infected cells, IBs appeared as small, disperse spherical puncta at up

to 12 h pi. Puncta of larger sizes and irregular shapes became more prevalent as the time of infection increased thereafter (Fig. 1B). By 24 h pi, nearly all infected cells contained at least one punctate structure larger than $3\ \mu\text{m}$ (the longest end-to-end distance) in addition to small spherical appearing puncta. The larger puncta were often irregularly shaped and positioned in a more central, perinuclear-like location (Fig. 1A). Irregularly shaped, large IBs were also observed by live-cell imaging (see reference 16) (Fig. 1B), as were found herein with formaldehyde-fixed HeLa cells (Fig. 1). Furthermore, similar irregularly shaped large IBs were seen with A549 cells as for HeLa cells following infection. These observations suggest the possibility that nascent MeV IBs may exist initially as small spheres that subsequently increase in size and adopt different shapes.

Measles virus N and P proteins are sufficient to mediate the formation of inclusion body-like puncta in transfected cells. We previously observed that complexes in MeV-infected cells containing viral N, P, L, and C proteins associated with the cellular WDR5 protein and together colocalized with infection-induced cytoplasmic inclusion bodies (16). These puncta represented sites distinct from known subcellular structures, including mitochondria, stress granules, endoplasmic reticulum (ER), *cis*-Golgi and *trans*-Golgi networks, and early and recycling endosomes (16). We now wished to test the formation of cytoplasmic IB puncta in transfected cells expressing MeV N and P proteins alone, independent of MeV replication. We focused initially on MeV N and P because studies exemplified by RABV (31), VSV (32), HMPV (38), and PIV3 (21) implicate the essential roles of their N and P proteins in their IB formation. In the case of RABV, N and P alone resulted in the formation of cytoplasmic IB recapitulating those seen in virus-infected cells (31).

We found that MeV N expressed alone in transfected cells mislocalized and was enriched in the nucleoli of 95% of the cells (Fig. 2A). Because N can bind cellular RNA and nucleoli contain high RNA content, we tested the possibility that N accumulated in the nucleoli due to its association with RNA. When three critical residues (K180, R194, and R354) shown to mediate the RNA binding activity of N (39) were mutated to alanine, this KRR/AAA mutant N protein was largely excluded from the nucleoli and displayed a diffuse nucleoplasm distribution in all cells (Fig. 2B). Expression of MeV P in the absence of N in transfected cells exhibited diffuse cytoplasmic staining in most (65%) of the cells (Fig. 2C, upper images), as previously reported (40). However, P expression alone also formed perinuclear puncta in 35% of the transfected cells (Fig. 2C, lower images). These puncta were rarely spherical and often displayed an unusually large size (Fig. 2C). In contrast, the characteristic spherical puncta seen in infected cells (Fig. 1A) were prevalent in transfected cells (95%) coexpressing both N and P (Fig. 2D). While it has been shown that P chaperones nascent N to prevent premature oligomerization and RNA binding of N (41, 42), our observation raised the possibility that MeV N might also chaperone P to prevent the formation of abnormal P complexes. The formation of spherical puncta in transfected cells coexpressing N and P did not depend on the ability of N to bind RNA since coexpression of the N(KRR/AAA) mutant and P resulted in puncta of comparable size and morphology as with the coexpression of wild-type (WT) N with P (Fig. 2E). Interestingly, similar to what was observed in MeV-infected cells (Fig. 1), in transfected cells, the punctum size increased, and their shape became more irregular with increased time after transfection in cells coexpressing N and P (Fig. 2F and G).

Inclusion bodies induced by measles virus infection and by N and P plasmid cotransfection fulfill the *in vivo* criteria for liquid-liquid phase separation. The spherical morphology of IBs induced by either MeV infection (Fig. 1) or by N and P plasmid cotransfection (Fig. 2) resembles protein droplets arising during liquid-liquid phase separation (LLPS). If these structures indeed were formed via LLPS, a characteristic behavior expected of them is the exchange of ingredients between the IBs and their aqueous environment. In addition, we would expect the IBs to undergo fusion and then for the fused structures to subsequently relax into a spherical shape as a result of the surface tension (34–37). To examine these criteria *in vivo*, we employed live cells stably expressing an EGFP or mCherry fusion of the cellular WDR5 protein. As reported

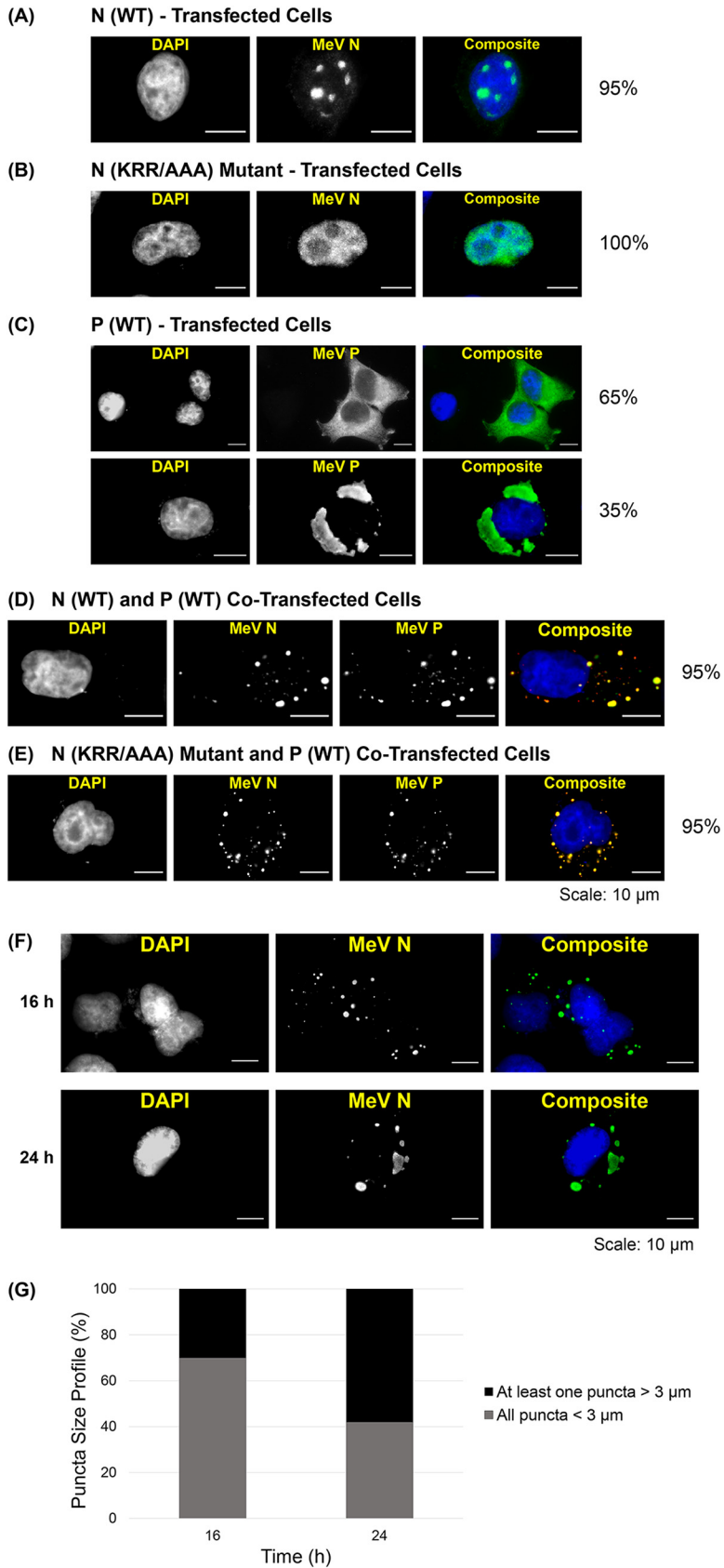


FIG 2 Measles virus N and P proteins are sufficient to mediate inclusion body formation. HeLa cells were transfected with plasmids expressing N alone, N(KRR/AAA) mutant alone, P alone, or cotransfected with (Continued on next page)

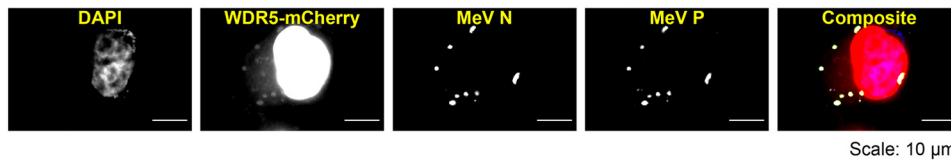
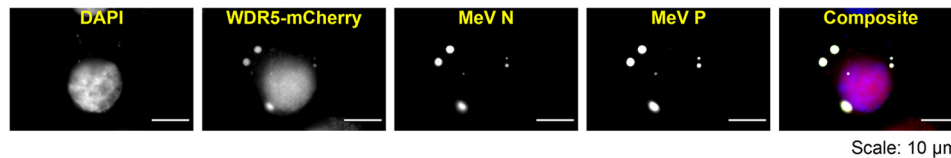
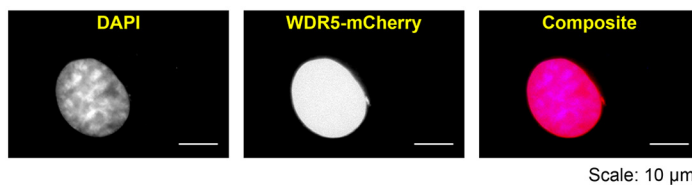
(A) Co-localization of N and P with WDR5 in Virus-Infected Cells**(B) Co-localization of N and P with WDR5 in Plasmid-Transfected Cells****(C) WDR5 Localization in Cells Uninfected and Not Transfected**

FIG 3 Colocalization of cellular WDR5 protein to inclusion bodies containing measles virus N and P proteins in virus-infected and plasmid-transfected cells. (A and B) HeLa cells stably expressing a mCherry fusion of WDR5 were either infected (MOI, 0.2) with isogenic Moraten vac2 virus with an HA-tagged L protein (A) or cotransfected with plasmids expressing wild-type N and P MeV proteins (B). After infection or transfection for 24 h, cells were fixed, immunostained for MeV N and P protein expression or stained with DAPI for DNA, and subjected to fluorescent imaging analysis. (C) Localization of WDR5-mCherry in uninfected cells not transfected is shown as a control. Scale bars = 10 μm.

earlier (16) and as shown herein, the WDR5 fusion was recruited to and concentrated within IBs formed both in MeV-infected cells (Fig. 3A) and N- and P-plasmid-cotransfected cells (Fig. 3B), thereby providing us with a framework by which we could assess IB dynamics in live cells by monitoring EGFP or mCherry fluorescence. In contrast, as a WDR5 fusion control, cytoplasmic IBs were not observed in cells uninfected and not transfected where WDR5-mCherry was nuclear (Fig. 3C).

To probe the exchange rate of IB-associated WDR5-EGFP, we performed fluorescence recovery after photobleaching (FRAP) analyses using cells either infected with MeV or cotransfected with N and P plasmids (Fig. 4). Under both conditions, infection (Fig. 4A) and cotransfection (Fig. 4B), we observed a rapid and efficient recovery after photobleaching for the small IBs (Fig. 4C). In contrast, the fluorescence recovery was inefficient for the large IBs (Fig. 4C), indicating that these structures had acquired a more gel-like property. It has been shown that, unlike the case of liquid droplets, most molecules within gel-like assemblies do not exchange with the surrounding cytoplasm (43). Importantly, the recovery efficiencies for puncta of similar sizes were comparable

FIG 2 Legend (Continued)

N (either wild-type or mutant) and P at 1:1 mass ratio. The N(KRR/AAA) mutant possesses alanine substitutions at three residues, K180, R194, and R354. Cells were fixed 24 h after transfection, immunostained for N and P proteins as indicated or stained with DAPI for DNA, and subjected to fluorescent imaging analysis. (A) Transfection with N alone forms puncta in nucleoli in 95% of transfected cells. (B) Transfection with N(KRR/AAA) mutant alone displays a diffuse nuclear staining in all (100%) of cells. (C) Transfection with P alone exhibits a mixed pattern, with a diffuse cytoplasmic localization in 65% of cells (upper) and large irregular-shaped perinuclear puncta in 35% of cells (lower). (D) Coexpression of wild-type N and P results in spherical IB-like puncta in 95% of infected cells. (E) Coexpression of N(KRR/AAA) mutant and P results in puncta similar to panel D with wild-type N. (A to E) The % values in represent averages from the results from three independent experiments with 500 transfected cells examined in each experiment. (F and G) Representative images (F) and IB size analysis (G) at 16 h and 24 h after transfection. The analysis of IB size was based on the longest path from two ends of the largest punctum in each cell, and a total of 500 cells were examined at each time point. Scale bars = 10 μm.

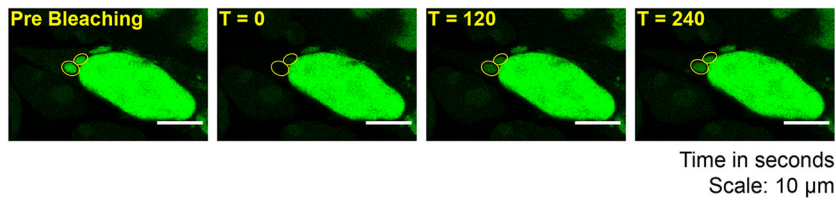
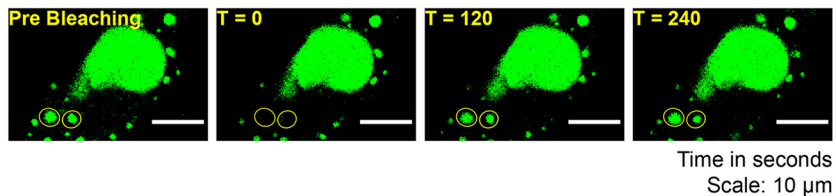
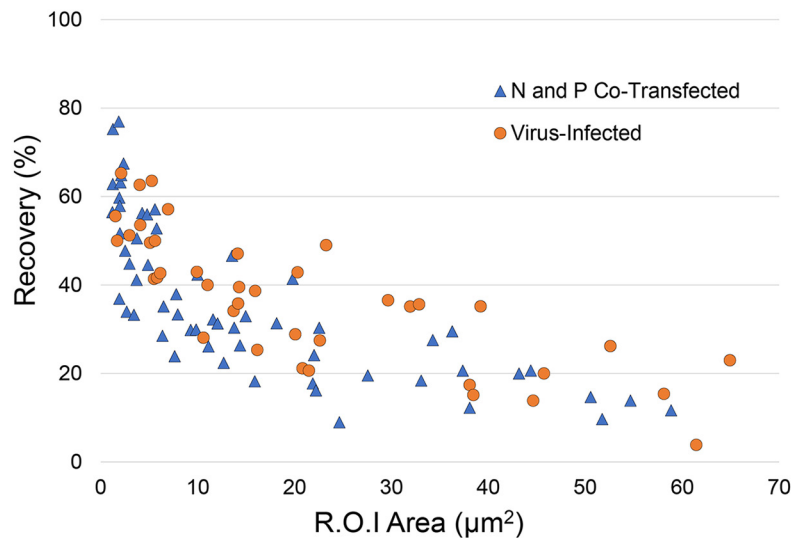
(A) Virus-Infected Cells**(B) N and P Plasmid-Transfected Cells****(C) Percent Recovery vs. Puncta Size**

FIG 4 Efficient exchange occurs between inclusion body-associated and cytosolic WDR5-EGFP, as determined by FRAP. (A and B) HeLa cells stably expressing an EGFP fusion of WDR5 were either infected (MOI, 0.2) with MeV (A) or cotransfected with N and P expression constructs (B). After 24 h, the fluorescence recovery after photobleaching (FRAP) was conducted on an individual punctum by drawing a region of interest (ROI; shown as a circle), using live-cell confocal microscopy. Each ROI was photobleached, and its fluorescent recovery was monitored for 4 min. Representative images of puncta from infected cells (A) and N- and P-cotransfected cells at prephotobleaching (B); photobleached (T = 0); and postphotobleaching (T = 120 and T = 240 s). (C) An inverse correlation between the punctum size and the percent recovery of fluorescent intensity. Red circles, MeV-infected cells; blue triangles, N- and P-cotransfected cells. Note that for a given punctum size, IB-associated WDR5-EGFP displays a comparable efficiency of photobleaching recovery between MeV-infected and N- and P-cotransfected cells.

between infected and transfected cells (Fig. 4C). Likewise, IBs induced both by MeV infection (Fig. 5A; see also Movie S1 in the supplemental material) and by N and P cotransfection (Fig. 5B) underwent fusion and relaxation. Thus, IBs triggered both by MeV infection and by N and P cotransfection not only shared similar time-dependent changes of size and morphology, but they also underwent fusion/relaxation and exhibited comparable photobleaching recovery efficiency of WDR5-EGFP fluorescence. Taken together, these data strongly suggest that the formation of IBs either by MeV infection or by N and P cotransfection is mediated via LLPS and lend further support to the notion that N and P proteins constitute core components of MeV IBs.

The C-terminal regions of N and P proteins of measles virus are crucial for inclusion body formation. Upon identification of N and P viral proteins functioning

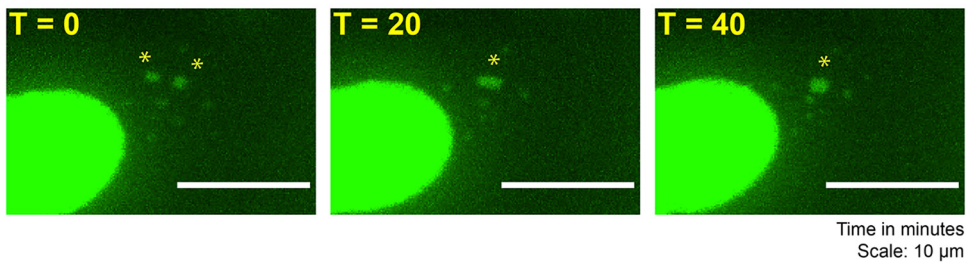
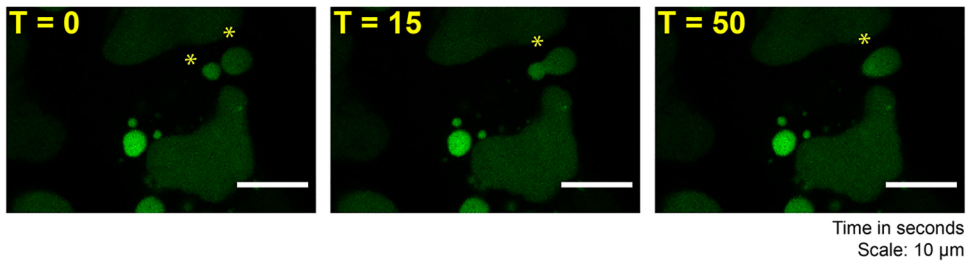
(A) WDR5-EGFP in Virus-Infected Cells**(B) WDR5-EGFP in N and P Plasmid-Transfected Cells**

FIG 5 Fusion and relaxation of inclusion bodies in MeV-infected and N- and P-cotransfected cells. (A and B) HeLa cells stably expressing an EGFP fusion of WDR5 were infected (MOI, 0.2) with MeV (A) or cotransfected with N and P expression constructs (B). Live-cell imaging was performed with time-lapse microscopy to track the fusion and relaxation of IBs (designated by asterisks) using WDR5-EGFP as the marker. Snapshots at different time points show the fusion and subsequent relaxation between two IBs in MeV-infected cells (A) and N/P-cotransfected cells (B).

together as minimal viral components sufficient to trigger MeV IB formation, we next attempted to gain insight into the regions of the proteins required for the IB assembly. The P protein is reported to interact with N in two ways (Fig. 6A). First, the N-terminal region (amino acids [aa] 1 to 60) of P can bind the core region (aa 1 to 391) of newly synthesized monomeric N to prevent premature association with cellular RNA and oligomerization (42). This RNA-free N is then transferred to the nascent ribonucleocapsid by an unknown mechanism during replication. Second, the C-terminal XD domain (aa 459 to 505) of P can also interact with the C-terminal MoRE motif (aa 489 to 506) located within the tail region of N (44). Because the second mode of N and P interaction is believed to anchor the viral polymerase L protein to the ribonucleocapsid during transcription and replication (45), we reasoned that it might be relevant to IB assembly and thus tested its role in the IB formation process using cells transfected with wild-type N and P or their mutants (Fig. 6).

Deletion of the XD domain of P prevented the formation of IB in 80% of transfected cells, as revealed by the comparison of truncated mutant P (aa 1 to 458) (Fig. 6C) to WT P (Fig. 6B), both in the presence of WT N. Moreover, mutation of three residues (L484, F497, and M500) to alanine within the C-terminal XD domain of P, residues known to be involved in the P binding of N (44), likewise impaired IB formation, albeit to a lesser extent, with only very small puncta detected in most (~70%) of the transfected cells (Fig. 6D). The somewhat weaker effect on IB formation conceivably might be due to a residual association activity between the MoRE domain of N and the mutated XD domain of P. Alternatively, the mutated XD may retain its ability to bind the core region of N, an interaction that has been previously reported (46). Compared to either deletion of XD or alanine substitution mutations within the XD domain of P protein, the deletion of the C-terminal MoRE-containing unstructured region from N (aa 392 to 525) produced the most dramatic phenotype. In nearly all transfected cells (97%), only a few small irregular-shaped puncta could be observed (Fig. 6E). Western blot analysis verified expression of the mutant and wild-type proteins of the predicted sizes and indicated that the observed effects of the mutations were not the consequence of reduced mutant protein levels (Fig. 6F). Based on these

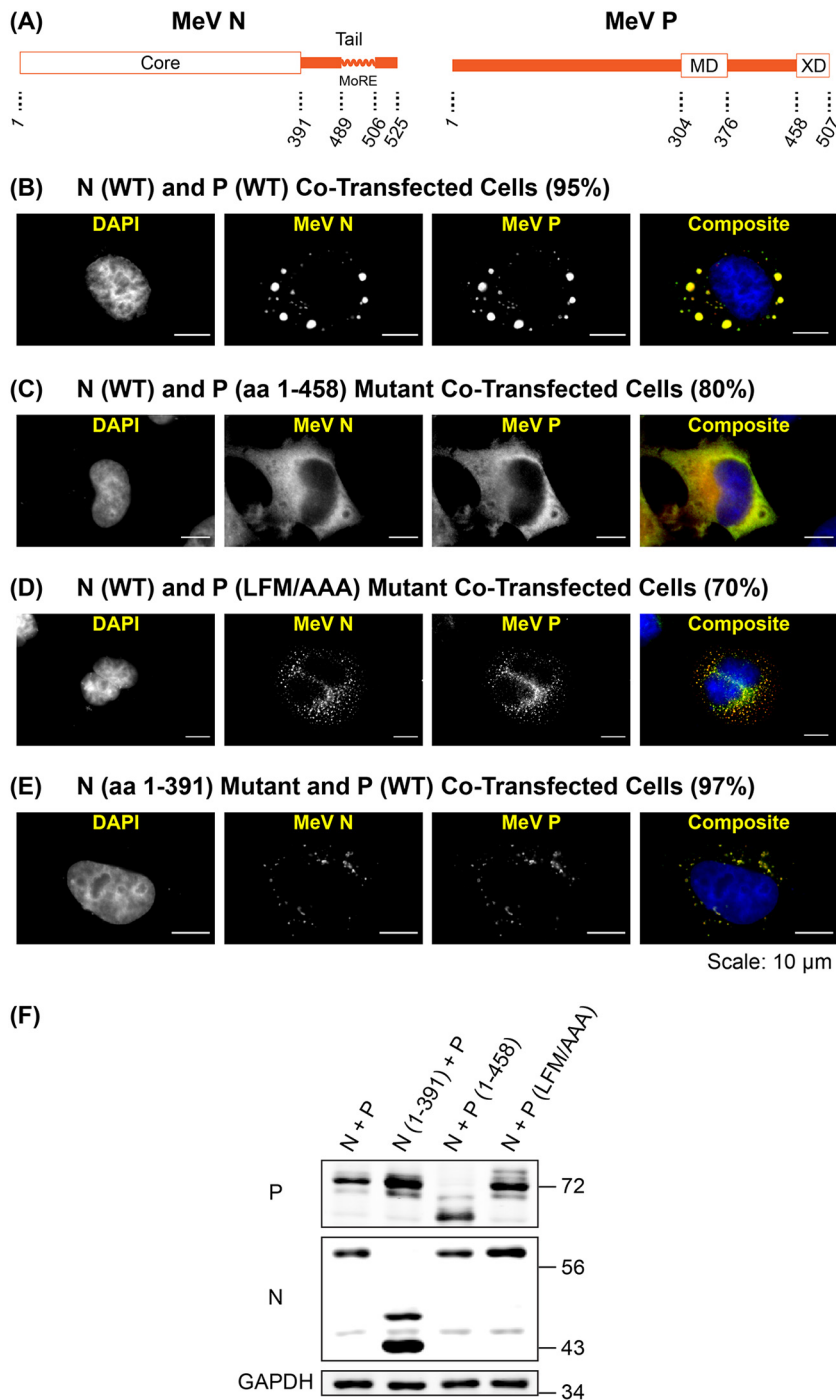


FIG 6 Mutational analysis identifies the C-terminal regions of measles virus N and P proteins as necessary for normal inclusion body formation. HeLa cells were cotransfected with N and P expression constructs, either wild-type or mutant, as indicated. Cells were fixed 24 h after transfection, immunostained for N and P proteins as indicated and stained with DAPI for DNA, and subjected to fluorescent imaging analysis. (A) Schematic diagram of MeV N and MeV P proteins with the amino acid positions of domains indicated. Structured and intrinsically disordered regions are indicated by boxes and solid lines, respectively. The MoRE motif located within the disordered region of N is represented by a helix. The MD and XD of P are the multimerization and X domains, respectively. (B to E) Representative images of IBs formed in cotransfected cells. The % values are averages of the results from three independent experiments, with 500 transfected cells examined in each experiment. Scale bars = 10 μ m. (B) Coexpression of N (WT) and P (WT). (C) Coexpression of N (WT) and XD deletion mutant P (aa 1 to 459). (D) Coexpression of N (WT) and substitution mutant P (LFM/AAA) containing alanine substitutions within the XD domain of P (L484A, F497A, and M500A). (E) Coexpression of deletion mutant N (aa 1 to 391) and P (WT). (F) Western blot analysis of cell lysates showing expression levels of N and P proteins; 34-, 43-, 56-, and 72-kDa molecular mass markers are indicated.

observations, we conclude that the XD domain of P and the C-terminal MoRE-containing unstructured region of N are pivotal regions for cytoplasmic IB formation triggered by these two viral proteins.

Phosphorylation of P protein affects inclusion body size. The measles virus P protein is phosphorylated at multiple sites. Among these, S86 and S151 are two major casein kinase 2 (CK2) phosphorylation sites, and their phosphorylation status is reported to change upon the binding of P to N (47, 48). We therefore explored using a combination of approaches whether these CK2 sites played a role in IB formation. As shown in Fig. 7A, treating MeV-infected cells with DMAT, a cell-permeable inhibitor of CK2, decreased the IB size (Fig. 7A, left) without significantly affecting N protein expression measured by Western analysis (Fig. 7A, right). To directly test the role of specific CK2 sites of P phosphorylation in IB assembly, we next examined whether the mutation of the serine residues at positions 86 and 151 to alanine also affected IB formation. The S86A/S151A phospho-site double mutant of P was expressed at a similar level as wild-type P protein (Fig. 7B), yet the S86A/S151A mutant compared to the WT P protein did not trigger the production of large IBs when coexpressed with N (Fig. 7C). The punctum size difference, illustrated by the cells shown in Fig. 7C, was verified by utilizing imaging software to quantify the fluorescent intensities of N and P proteins and the volumes of the largest puncta of individual cells. When cells that displayed comparable levels of N and P between the control and experimental groups were analyzed, the volume of the largest punctum within each cell was significantly reduced for the phospho-site S86A/S151A mutant of P (Fig. 7D), further indicating a role for S86 and S151 phosphorylation in modulating the size of IBs formed by N and P coexpression.

Dynein-mediated transport promotes the formation of large MeV inclusion bodies and enhances viral replication. Whereas the small IBs were observed scattered throughout the cytoplasm of MeV-infected cells, the large IBs were often seen positioned in a more central location near the cell nucleus, as illustrated in Fig. 1. This observation led us to consider whether the small IBs possibly were transported along microtubules toward the cell nucleus where they then undergo fusion to generate the large IBs. To test this, we assessed the effect of HPI-4, a cell-permeable specific inhibitor of dynein motor function (49), on the size and spatial distribution of MeV IBs and on viral titer. First, we examined the effect of HPI-4 drug treatment at increasing concentrations, 20, 40, and 80 μ M, beginning at 12 h pi when the IBs were still small and uniformly distributed (Fig. 1) and then continuing until the time of analysis at 18 h pi. As shown in Fig. 8A, all three concentrations of HPI-4 reduced the fraction of infected cells that possessed at least one large IB punctum, with the greatest effect seen at 80 μ M. Consistent with this observation, compared to the infected control cells that were not drug treated, cells treated with 80 μ M HPI-4 exhibited a strikingly different IB pattern, with the vast majority of IBs being smaller and uniformly distributed throughout the cytoplasm (Fig. 8B). The volume measurement of the largest punctum within a cell confirmed the inhibitory effect of HPI-4 on the formation of large IBs (Fig. 8C). Importantly, HPI-4 also led to lower levels of viral protein expression without significantly affecting the level of glyceraldehyde-3-phosphate dehydrogenase (GAPDH) or alpha-tubulin (Fig. 8D). Moreover, viral titers were decreased \sim 30-fold following treatment with 80 μ M HPI-4. Finally, similar HPI-4 effects on the IB size and distribution were also observed after treatment with dynarrestin (Fig. 8E), a drug that inhibits dynein by a mechanism different from that of HPI-4 (50). Taken together, these data are consistent with the notion that dynein promotes viral replication by facilitating the formation of large IBs.

DISCUSSION

The presence of membrane-bound organelles is a hallmark of eukaryotic cells. While a permeability barrier provided by a membrane offers several advantages to cells, eukaryotic cells also contain organelles that are not enclosed by membranes. Recent studies with rhabdoviruses have established that the formation of membraneless

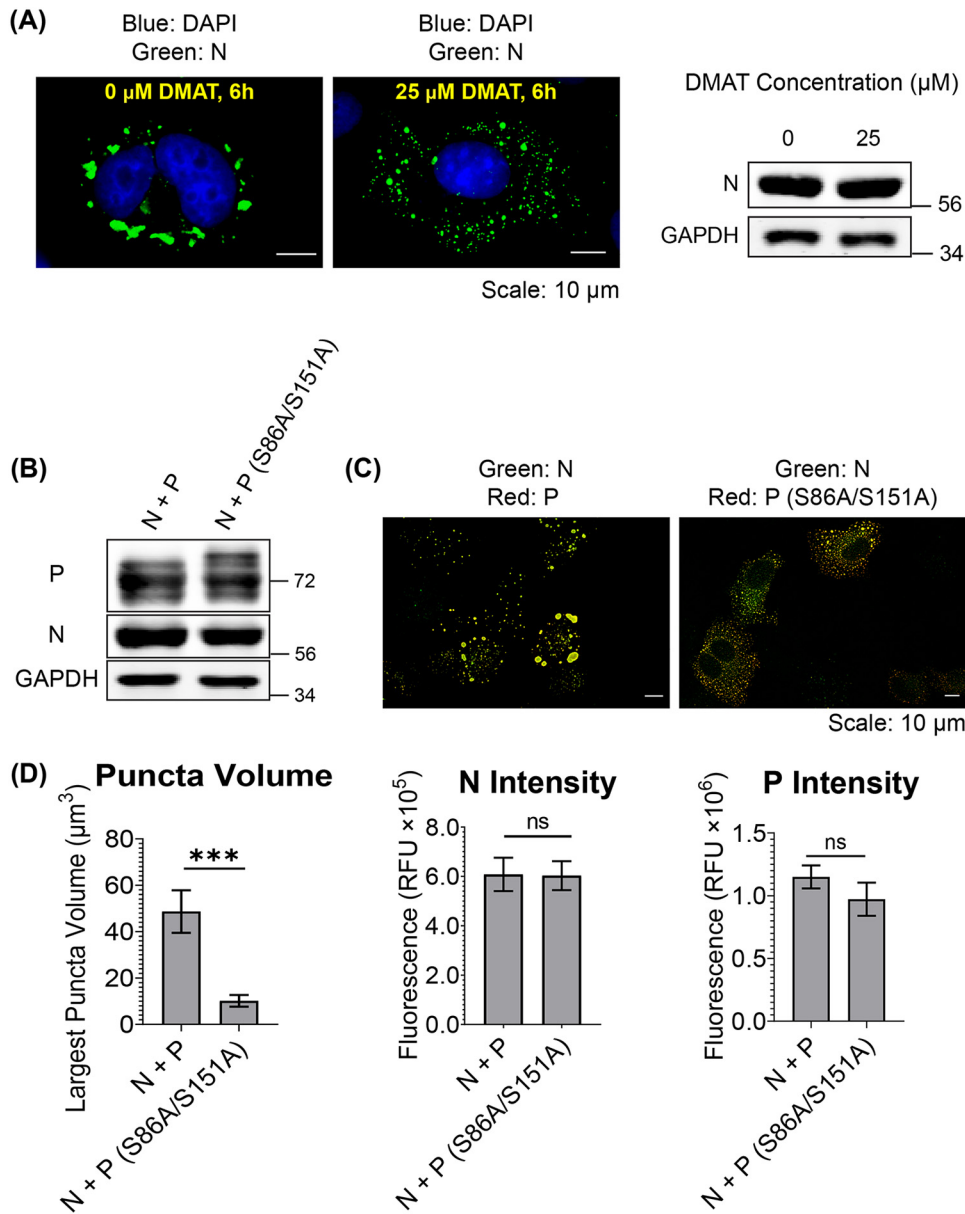


FIG 7 Phosphorylation of measles virus P protein modulates inclusion body size. HeLa cells were infected with MeV or cotransfected with N and P expression constructs. Cells were fixed after infection (18 h) or transfection (24 h), immunostained for N and P proteins or stained with DAPI for DNA, as indicated, and subjected to fluorescent imaging analysis. (A) Cells were infected (MOI, 0.2) and at 12 h after infection were treated with the casein kinase 2 inhibitor DMAT or the solvent DMSO vehicle for 6 h before fixation and immunostained for N protein (left). The level of N was also determined by a Western blot assay (right). (B) Western blot analysis of expression levels of wild-type N and P and the CK2 phosphorylation site double-substitution mutant, P(S86A, S151A); 34-, 56-, and 72-kDa molecular mass markers are indicated. (C) Representative confocal images of N and P cotransfection puncta formed with wild-type N plus either wild-type or mutant P(S86A, S151A). Scale bars = 10 μ m. (D) The cellular expression levels of N and P proteins for cells transfected with N and P or N and mutant P(S86A, S151A) were quantified using the Imaris three-dimensional (3D) reconstruction software (represented by relative fluorescent units [RFU]). For each group, 25 cells exhibiting similar N and P levels were selected for further analysis. The volumes of the largest puncta found in each of the 25 cells were measured for both groups and averaged. The error bar represents the standard error of the mean. ***, $P < 0.001$.

compartments can be triggered by viral infection and is mediated by a process called liquid-liquid phase separation (LLPS) (31, 32). Herein, we provide three lines of evidence that measles virus inclusion bodies, membraneless viral factories (16), are formed via LLPS. First, nascent IBs adopt a spherical shape observed during the early phase of infection (Fig. 1). Second, using EGFP-tagged WDR5, a cellular protein that was previ-

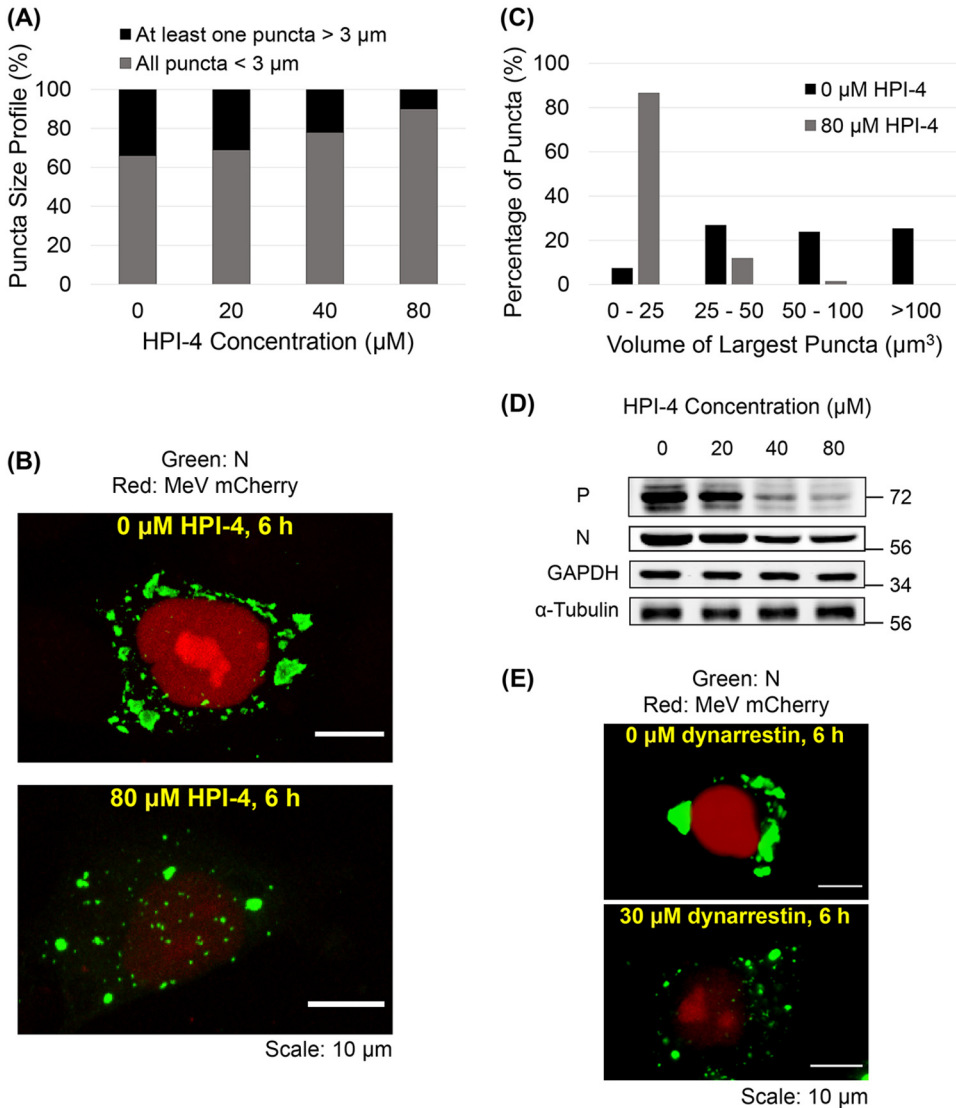


FIG 8 Dynein-mediated transport promotes the formation of large inclusion bodies in measles virus-infected cells. HeLa cells at 12 h after infection (MOI, 0.2) were treated with a dynein inhibitor, either HPI-4 or dynarrestin, at the indicated concentrations for 6 h before confocal microscopy analysis. (A) The size profile of the largest punctum present in each infected cell treated with increasing concentrations of HPI-4, as indicated. Punctum size was measured as the longest path from two ends of the largest punctum in each cell. A total of 500 cells were examined under each condition. (B) Representative images of cells either untreated or treated with 80 μM HPI-4. Scale bars = 10 μm. (C) Volumes of the largest punctum found in individual cells were measured using the Imaris 3D reconstruction software. A total of 55 cells were examined under each condition. (D) Western blot analysis of lysates prepared from untreated and HPI-treated cells for N and P expression; GAPDH and α-tubulin are included for loading controls; 34-, 56-, and 72-kDa molecular mass markers are indicated. (E) Representative images of cells either untreated or treated with 30 μM dynarrestin. Scale bars = 10 μm.

ously established (16) as a host marker of viral IBs (Fig. 3A), we showed by live-cell imaging that these small, rounded IBs undergo fusion and relaxation resulting in the formation of large IBs (Fig. 5A). Third, the fluorescent signal of IB-associated WDR5-EGFP was recovered following photobleaching (Fig. 4A), consistent with a dynamic exchange of components between IBs and their environment. Utilization of WDR5-mCherry and WDR5-EGFP as reporters in analyses of IB formation offered the advantage by eliminating the need to add a fluorescent tag to a viral protein that could potentially adversely affect the biogenesis or dynamics of IBs.

Utilizing a transfection-based reconstitution assay, we further demonstrated that N

and P proteins are two viral components that drive MeV-induced IB formation in the absence of viral replication (Fig. 2, 3B, 4B, and 5B). Moreover, interactions involving the C-terminal regions of N and P seemed pivotal to the LLPS process (Fig. 6). Interestingly, whereas an RNA-protein interaction is often described in LLPS (34–37, 51), our results showed that formation of N and P-mediated IB likely did not depend on the ability of N to bind RNA based on the K180A, R194A, R354A triple mutant phenotype (Fig. 2E). In addition, the phosphorylation of P modulated the efficiency of IB assembly as revealed by serine-to-alanine mutagenesis of two key phosphorylation sites (S86 and S151) in the P protein (Fig. 7). In MeV-infected cells, the P gene also encodes two accessory proteins, V by a pseudotemplated G addition by the viral RNA polymerase (pol) L, and C by an alternative translation start (1, 52). In our studies, the P plasmid construct was mutated to eliminate C expression, and cellular RNA pol II does not generate the edited RNA with an inserted G that encodes V. Therefore, the effects seen with the P construct transfections were due to P protein expression. Finally, the inhibition of dynein motor activity altered the spatial distribution of MeV IBs and greatly reduced their size, with a concomitant decreased production of viral proteins and infectious virus (Fig. 8). These results provide novel insights into the formation and function of MeV-induced inclusion bodies by LLPS. Our findings may be related to two recent reports (31, 32) concerning the ability of *Mononegavirales* members of the *Rhabdoviridae* family to trigger the formation of cytoplasmic inclusion bodies, sites of viral replication, by a liquid-liquid phase separation process.

LLPS was shown to mediate the formation of IBs in cells infected with RABV (31) and VSV (32). Our observation that MeV IBs exhibit properties of liquid organelles indicates that LLPS also underlies IB formation in the case of a *Paramyxoviridae* family member. It is noteworthy that some viral proteins, illustrated by N and P proteins of MeV, RABV, and VSV that trigger IB formation, contain a high content of intrinsic disordered regions (IDRs) (53). The presence of structural disorder is thought to mitigate a potentially deleterious impact caused by mutations resulting from viral RNA polymerase errors, and hence to confer flexibility and adaptability to viral protein function, including interaction with the host innate immune system (54). Our findings described herein, taken together with those of others (31, 32), raise the possibility that the prevalence of structural disorder within viral proteins also empowers negative-strand RNA viruses to assemble their replication factories via LLPS. Viral inclusions are also observed in the nuclei of cells infected by some DNA viruses (55); it will be interesting to determine whether LLPS contributes as well to the formation of these nuclear inclusion structures.

The ability to reconstitute IB assembly in the absence of viral replication by coexpression of MeV N with P in transfected cells provided an experimental approach to assess the domain regions of N and P involved in the IB formation. In agreement with the finding by Nikolic et al. (31) that the deletion of the ~100 residues of RABV P protein involved in its interaction with N abolished the formation of IBs, we also observed that the formation of IB in cells coexpressing MeV N and P proteins was severely compromised (Fig. 6) after substitution mutations within XD domain of P at positions established to make direct contact with the MoRE motif of N (44). These results lend support to the conclusion that the binding of N and P within their C-terminal regions is essential for IB formation with MeV. Whereas similarities exist in the IB assembly of *Paramyxoviridae* and *Rhabdoviridae*, there are also differences as described below.

First, MeV N and P proteins (525 and 507 aa, respectively) are somewhat larger than their RABV counterparts (450 and 296 aa, respectively), with the increased sizes mainly due to the presence of longer IDRs (54, 56). It is well established that IDRs can confer multivalent weak interactions that are characteristic of LLPS (34–37). MeV N contains an IDR (~130 aa) located at its C terminus (54), whereas RABV N has a much shorter IDR (~30 aa) present in the middle region of N protein (56). Likewise, the N-terminal IDR of MeV P (~300 aa) is significantly longer than that present in the RABV and VSV P proteins (~100 aa) (54, 56). In addition, whereas MeV P forms a tetramer (57), RABV and VSV P proteins are reported to exist as dimers (58). These differences in the quaternary structure of the P proteins may influence the multivalence of protein interactions.

Therefore, it seems likely that the assembly of MeV IBs compared to that of RABV and VSV IBs involves unique kinds of interactions.

The presence of the longer IDRs in the MeV proteins may expand the diversity of mechanisms that regulate the assembly/disassembly processes of viral IBs. This possibility is supported by the following observations. First, the IDR of MeV N protein spans the region of aa 392 to 525, which includes the XD-interacting MoRE domain (Fig. 7). Deletion of this IDR to generate the truncated N protein corresponding to aa 1 to 391 exhibited a more severe defect in the assembly of IBs relative to the XD deletion mutant of MeV P (Fig. 6). This finding implies that, in addition to interaction with the XD domain of P, the IDR of N likely has additional functions in IB formation. It is intriguing that the same IDR has been suggested recently by others to regulate the paramyxovirus transcription gradient, independent of its ability to bind P (59). A similar IDR found in a closely related virus, canine distemper virus (CDV), regulates CDV transcription and pathogenesis (60). Recombinant MeV expressing an N mutant protein that lacks the central region of IDR, but retains its ability to bind P, displays a temperature-sensitive growth phenotype (59). Since LLPS is known to be very sensitive to temperature (34–37), it would be worthwhile to test whether the above-mentioned temperature-sensitive phenotype is accompanied by a defective organization of IBs.

Second, although the phosphorylation of RABV P protein does not affect IBs (31), we found through use of a pharmacologic CK2 kinase inhibitor and also by mutation of phosphorylation sites that phosphorylation of MeV P modulated the size of IBs (Fig. 7). Interestingly, the dynamic phosphorylation and dephosphorylation of VP30, a protein essential for EBOV life cycle, are reported to occur within IBs (61). We are currently investigating how CK2-mediated phosphorylation of MeV P alters IB biogenesis. Compared to the MeV wild-type P protein, mutant P produced an additional band of higher molecular weight (MW), presumably due to a yet-to-be characterized covalent modification. Third, our finding that N and P constitute the minimal system to form MeV IB-like structures (Fig. 2) is consistent with the earlier observation that MeV P retains N in the cytoplasm (40), and similar to our finding, coexpression of N and P is also sufficient to generate structures recapitulating RABV IBs (31). On the other hand, simultaneous expression of N, P, and L is required for the production of VSV IB-like structures (32). Fourth, unlike RABV and VSV P genes, the MeV P gene encodes two additional accessory proteins, C and V, both of which are found associated with MeV IBs (16) and affect innate immunity (12, 52). Furthermore, since M protein mediates the assembly of virus particles by linking mature RNP to the membrane glycoproteins (9), it too may interact with IBs. In the case of Nipah virus, Ringel et al. (20) recently reported the formation of two types of IB in infected Vero cells, one located at the perinuclear region and lacking M protein, and the other near the plasma membrane and containing M. Interestingly, unlike our findings with MeV in which perinuclear IBs were observed at late time points in both infected and transfected cells (Fig. 1 and 2F and G), the perinuclear NiV IB appeared prior to the plasma membrane-associated IB in both infected and transfected cells. Conceivably different viruses within the *Paramyxoviridae* family have evolved distinct strategies to couple IBs to their life cycles.

Our observation that dynein inhibition impairs viral protein and infectious virus production and formation of larger IBs suggests that, compared to small IBs, large IBs potentially are beneficial to MeV replication (Fig. 8). Conceivably, the smaller nascent IBs can move easily by diffusion due to their smaller size and fuse with each other in a dynein-independent manner. However, as they increase in size, the diffusion becomes slower, thereby limiting the fusion efficiency. The dynein motor may possibly promote the formation of large IBs by transporting IBs from the cell peripheral regions toward the cell center where their fusion is facilitated because of the higher local IB density. The literature indicates that LC8, a dynein light chain, can bind P proteins from some negative-strand RNA viruses, including RABV (62, 63), Mokola (64), and EBOV (65). It remains to be determined whether the dynein transport function also promotes the formation of large IBs in the case of these negative-strand viruses. Whereas we favor a model by which dynein facilitates large

IB formation via its classical transport activity, we cannot rule out the possibility that it does so by unconventional mechanisms (66). Another important question concerns the mechanism by which large IBs seemingly promote viral replication. In theory, the component concentrations should remain comparable after the fusion and relaxation of two IBs, rendering it less likely that the growth advantage is a result of viral protein concentration. One possibility that we are exploring is that a large IB more efficiently shields the viral components from innate immune surveillance responses (12, 13, 67), a hypothesis consistent with the gel-like property of large IBs (Fig. 4C). Another possibility is that the composition and cellular environment of large IBs are distinct from those of small IBs. Considering that the dynein motor inhibitor was present between 12 and 18 h pi in the MeV-infected cells, it is tempting to speculate that the decreased levels of viral proteins and titers observed in the inhibitor-treated compared to untreated cells potentially resulted from impaired secondary viral transcription and replication, as opposed to defective virion assembly.

In summary, liquid-liquid phase separation mediates the formation of many membraneless organelles in mammalian cells and has recently become a topic of intense investigation (33–37, 51). As shown herein and by others (31, 32), negative-strand RNA viruses trigger the formation of IBs with properties of liquid organelles by employing LLPS. Identification and characterization of the domain factors and modifications, including phosphorylation, involved in regulating the assembly/disassembly of these viral IBs are critical next steps and may provide insights into novel antiviral strategies. Moreover, compared to other complex membraneless compartments, such as nucleoli and stress granules, the viral IBs may serve as a simpler model organelle for studying LLPS processes.

MATERIALS AND METHODS

Virus. Recombinant vac2 MeV isogenic to the Moraten vaccine strain and expressing the mCherry with a nuclear localization signal (mCherryNLS) (68) or N-terminally hemagglutinin (HA)-tagged L protein (16) have been described. Virus rescue, stock generation, and titration were performed as previously described (69, 70).

Cells. HeLa cells were cultured in advanced Dulbecco's modified Eagle medium (DMEM; HyClone DMEM-RS) supplemented with 4% (vol/vol) fetal bovine serum (Atlanta Biologicals), 2 mM glutamine (Life Technologies), and penicillin (100 μ g/ml)-streptomycin (100 units/ml; Life Technologies). HeLa cells stably expressing WDR5-EGFP (71) or WDR5-mCherry (this study) were grown in the same medium with an additional supplement of 3 μ g/ml puromycin. Cells were dissociated for passage using trypsin (0.25%)–EDTA (0.1%) (HyClone). Virus infections were carried out at a multiplicity of infection of 0.2 or at 5 50% tissue culture infective dose (TCID₅₀) per cell, as indicated in the figure legends.

DNA constructs and transfection. Plasmids pCAGGS-N and pCAGGS-P contain the N and P open reading frames (ORFs) cloned into the NotI/NheI and EcoRI/XhoI sites of pCAGGS, respectively (generously provided by Christian Pfaller and Roberto Cattaneo, Mayo Clinic). The P construct contains two silent mutations in the P ORF, CAT to CAC at His8 and CTG to CTA at Leu13. The first mutation abolishes the alternative AUG translation site for the C ORF, and the second mutation introduces a termination codon after the 5th amino acid of the C ORF. For pCAGGS-N(1-391) and pCAGGS-P(1-458), the truncated fragments were amplified by PCR using Phusion polymerase (catalog no. F-553L; Thermo Fisher) and inserted into the EcoRI/BglII and EcoRI/XhoI sites of pCAGGS, respectively. The S86A and S151A mutations were introduced to pCAGGS-P using PCR mutagenesis. Likewise, the L484A/F493A/M500A mutant of P and the K180A/R194A/R354A mutant of N were prepared by PCR mutagenesis. All point mutant and deletion mutant constructs were verified by the sequencing analysis. The plasmids were then transfected into cells using TurboFect transfection reagent (catalog no. R0531; Thermo Fisher) at a ratio of 3 μ l of TurboFect per μ g of DNA.

Reagents and antibodies. The reagents used for cell culture are as follows: DMAT (catalog no. A336810; Apexbio Biotechnology, 10 mM stock in dimethyl sulfoxide [DMSO]), HPI-4 (catalog no. 4529; Tocris Biosciences, 50 mM stock in DMSO), and dynarrestin (catalog no. 6526; Tocris Biosciences, 10 mM stock in DMSO). The primary antibodies used for Western blot (WB) analysis and immunofluorescence (IF) are as follows: rabbit anti-MeV N₅₀₅ (IF, 1:2,500; WB, 1:4,000) (52), rabbit anti-MeV P₂₅₄ (IF, 1:2,500; WB, 1:4,000) (52), rabbit anti-MeV N₁₂ (IF, 1:2,500; WB, 1:4,000) (72), mouse anti-GAPDH (Biochain Institute no. Y3322GAPDH; WB, 1:4,000), and mouse anti- α -tubulin (SCBT no. 23948; WB, 1:2,000).

Cell lysis and SDS-PAGE and Western blotting. Cell lysates were made using ice-cold RIPA buffer (50 mM Tris-HCl [pH 8.0], 150 mM NaCl, 1% NP-40, 0.5% sodium deoxycholate, and 0.1% SDS) supplemented with 1 \times protease inhibitor cocktail (catalog no. 14002; Biotool), 1 \times phosphatase inhibitor cocktail (catalog no. 15002; Biotool), and 5 mM EDTA. Protein concentration was determined using the CB-X protein assay, and an equal amount of total protein was analyzed by SDS-polyacrylamide gel electrophoresis (6% to 15% gels, depending on the proteins to be resolved).

Proteins were transferred to Immobilon-FL 0.45- μ m polyvinylidene difluoride (PVDF) membranes (catalog no. IPFL00010; Millipore) using an Owl HEP-1 semidry electroblotting system (Thermo Scientific). Membranes were incubated overnight at 4°C with the appropriate primary antibody diluted in a 1:1 mixture of Odyssey blocking buffer (Li-Cor Biosciences) and PBST (1 \times PBS supplemented with 0.1% Tween 20). Membranes were washed with PBST (3 \times , 10 min each), incubated in the dark for 45 min with the appropriate secondary antibody [goat anti-mouse or anti-rabbit IgG (H+L) DyLight 680 conjugated; Thermo Scientific], washed with PBST (three times, 5 min each), followed by PBS for 5 min, and dried in the dark. Fluorescence imaging and quantification were performed on an Odyssey infrared imaging system (Li-Cor Biosciences).

Immunofluorescence. Cells grown on coverglass (catalog no. 72230-1; Electron Microscopy Sciences) were fixed in 3% UltraPure electron microscopy (EM)-grade formaldehyde (catalog no. 04018-1; Polysciences, Inc.) in PBS for 10 min at 24 h after MeV infection or DNA transfection, unless otherwise noted, quenched with PBS containing 100 mM glycine (2 \times , 5 min each), and permeabilized with PBS containing 0.1% Triton X-100 for 15 min. Fixed cells were blocked in BLOK casein in PBS (catalog no. 786-194; G-Biosciences) containing 5% normal goat serum (catalog no. 005-000-121; Jackson ImmunoResearch Laboratory) for 30 min, incubated with primary antibody diluted in blocking buffer for 3 h, washed in PBS (3 \times , 5 min each), incubated in fluorophore-conjugated secondary antibody diluted in blocking buffer for 1 h, washed in PBS (3 \times , 5 min each), incubated in PBS containing 1 μ g/ml DAPI for 5 min, and washed in PBS (3 \times , 2 min each). Coverslips were then allowed to air dry in the dark and mounted in PPD antifade (90% glycerol, 10% PBS, 1 mg/ml *p*-phenylenediamine [pH 8.0]). The following secondary antibodies were used at a dilution of 1 to 200: goat anti-mouse IgG (Alexa Fluor 488 no. 115-545-062, rhodamine red-X no. 115-295-062, and Alexa Fluor 647 no. 115-605-146; Jackson ImmunoResearch Laboratory) and goat anti-rabbit IgG (Alexa Fluor 488 no. 111-545-144, rhodamine red-X no. 111-295-144, and Alexa Fluor 647 no. 111-605-144; Jackson ImmunoResearch Laboratory).

Epifluorescence microscopy. Slides were imaged using an Olympus IX81 motorized inverted fluorescence microscope with a Plan-Apochromat 60 \times oil total internal reflection fluorescence objective (numerical aperture [NA], 1.45; Olympus), Semrock excitation and emission filters, and an X-Cite Exacte illumination source (Lumen Dynamics Group, Inc.). Images were captured using a monochrome digital camera (Evolution QEi; Media Cybernetics) controlled with In Vivo acquisition software, v.3.2.0 (Media Cybernetics). Image analysis was performed using ImageJ (NIH) and Adobe Illustrator.

Confocal fluorescence microscopy. Immunostained slides were imaged on a Leica TCS SP8 X confocal laser resonant scanning microscopy platform using a Leica DMI8 inverted confocal microscope. A high-contrast (HC) PL Apo 63 \times objective (NA, 1.4 oil; Leica) was used throughout, with excitation laser lines at 405 nm, 488 nm, 559 nm, and 635 nm for DAPI, EGFP, mCherry/rhodamine red-X, and Cy5-conjugated secondary antibody, respectively. Images were captured as z-stacks (0.5- μ m steps). All live-cell imaging experiments on the DMI8 confocal microscope were performed at 37°C on an HC PL Apo 63 \times objective (NA, 1.3 glycerol; Leica). Cells were grown on Matrigel-coated (1:500) glass-bottomed Delta T dishes (Biotechs). A top stage incubator integrated system (Bold Line H301 T; Okolab) and heating/cooling circulating bath (Lauda ECO RE 415 S; Lauda-Brinkmann) were controlled by Oko-Touch (Okolab) for chamber heating and 5% CO₂ perfusion. Unless otherwise specified, live-cell imaging was conducted at 24 h postinfection.

FRAP analysis. WDR5-EGFP dynamics among inclusion bodies in MeV-infected cells and N- and P-plasmid-cotransfected cells were analyzed using fluorescence recovery after photobleaching (FRAP) provided through the Leica Application Suite X software, v.3.5.5.19976 (Leica Microsystems). Prebleach images of inclusion bodies were collected prior to the phase of photobleaching. Following photobleaching (70% laser intensity for 50 s) of the region of inclusion bodies or puncta, the postphotobleaching recorded the fluorescence recovery of the photobleached area over time (5% laser intensity for 245 s). Using 5% laser intensity for the same duration of FRAP had negligible photobleaching onto the samples. A profile plot (intensity versus time) of all phases was constructed for the EGFP channel, where the percent recovery was calculated by the intensity at the end of recording over the prebleach intensity.

Quantification of punctum characteristics. Quantification of IB characteristics was done with Imaris x64 v.9.2.1 (BitPlane) using the Surfaces feature. Selection for the surface was based on absolute intensity threshold, in which only puncta of a certain length in micrometers were highlighted. Metadata of the Surfaces analysis contained the surface area (in square micrometers), volume (in cubic micrometers), and relative fluorescence intensity unit among each highlighted puncta.

Statistical analysis. Statistical significance was assessed by unpaired Student's *t* test, and Fig. 7D data are presented as means, with error bars indicating the standard error of the mean (SEM).

SUPPLEMENTAL MATERIAL

Supplemental material for this article may be found at <https://doi.org/10.1128/JVI.00948-19>.

SUPPLEMENTAL FILE 1, AVI file, 2.8 MB.

SUPPLEMENTAL FILE 2, PDF file, 0.1 MB.

ACKNOWLEDGMENTS

We acknowledge the use of the NRI MCDB Microscopy Facility and the Resonant Scanning Confocal supported by the NSF MRI grant DBI-1625770, research grant

AI-20611 to C.E.S. from the National Institute of Allergy and Infectious Diseases, NIH, UC Santa Barbara Undergraduate Research and Creative Activities (URCA) grants to D.M., and a fellowship to Y.Z. from China Scholarship Council.

We are grateful to Christian Pfaller and Max Wilson for their helpful suggestions and comments.

We declare no conflicts of interest.

D.M. and C.E.S. designed the experiments and wrote the manuscript, and D.M., Y.Z., and J.M.S. performed the experiments.

REFERENCES

- Lamb RA, Parks GD. 2013. Paramyxoviridae, p 957–995. In Knipe DM, Howley PM, Cohen JI, Griffin DE, Lamb RA, Martin MA, Racaniello VR, Roizman B (ed), *Fields virology*, 6th ed, vol 1. Lippincott Williams & Wilkins, Philadelphia, PA.
- Cattaneo R, Donohue RC, Generous AR, Navaratnarajah CK, Pfaller CK. 2019. Stronger together: multi-genome transmission of measles virus. *Virus Res* 265:74–79. <https://doi.org/10.1016/j.virusres.2019.03.007>.
- Dabbagh A, Patel MK, Dumolard L, Gacic-Dobo M, Mulders MN, Okwo-Bele J-M, Kretsinger K, Papania MJ, Rota PA, Goodson JL. 2017. Progress toward regional measles elimination—worldwide, 2000–2016. *MMWR Morb Mortal Wkly Rep* 66:1148. <https://doi.org/10.15585/mmwr.mm6642a6>.
- Griffin D. 2013. Measles, p 1042–1069. In Knipe DM, Howley PM, Cohen JI, Griffin DE, Lamb RA, Martin MA, Racaniello VR, Roizman B. (ed), *Fields virology*, 6th ed, vol 1. Lippincott Williams & Wilkins, Philadelphia, PA.
- Bourhis J-M, Johansson K, Receveur-Bréchet V, Oldfield CJ, Dunker KA, Canard B, Longhi S. 2004. The C-terminal domain of measles virus nucleoprotein belongs to the class of intrinsically disordered proteins that fold upon binding to their physiological partner. *Virus Res* 99: 157–167. <https://doi.org/10.1016/j.virusres.2003.11.007>.
- Kingston RL, Hamel DJ, Gay LS, Dahlquist FW, Matthews BW. 2004. Structural basis for the attachment of a paramyxoviral polymerase to its template. *Proc Natl Acad Sci U S A* 101:8301–8306. <https://doi.org/10.1073/pnas.0402690101>.
- Curran J, Kolakofsky D. 1999. Replication of paramyxoviruses. *Adv Virus Res* 54:403–422. [https://doi.org/10.1016/S0065-3527\(08\)60373-5](https://doi.org/10.1016/S0065-3527(08)60373-5).
- Longhi S. 2009. Nucleocapsid structure and function. *Curr Top Microbiol Immunol* 329:103–128.
- Cox RM, Plemper RK. 2017. Structure and organization of paramyxovirus particles. *Curr Opin Virol* 24:105–114. <https://doi.org/10.1016/j.coviro.2017.05.004>.
- Cattaneo R, Kaelin K, Baczkó K, Billeter MA. 1989. Measles virus editing provides an additional cysteine-rich protein. *Cell* 56:759–764. [https://doi.org/10.1016/0092-8674\(89\)90679-x](https://doi.org/10.1016/0092-8674(89)90679-x).
- Bellini W, Englund G, Rozenblatt S, Arneiter H, Richardson C. 1985. Measles virus P gene codes for two proteins. *J Virol* 53:908–919.
- Randall RE, Goodbourn S. 2008. Interferons and viruses: an interplay between induction, signalling, antiviral responses and virus countermeasures. *J Gen Virol* 89:1–47. <https://doi.org/10.1099/vir.0.83391-0>.
- Pfaller CK, Li Z, George CX, Samuel CE. 2011. Protein kinase PKR and RNA adenosine deaminase ADAR1: new roles for old players as modulators of the interferon response. *Curr Opin Immunol* 23:573–582. <https://doi.org/10.1016/j.coi.2011.08.009>.
- Tawara JT, Goodman JR, Imagawa DT, Adams JM. 1961. Fine structure of cellular inclusions in experimental measles. *Virology* 14:410–416. [https://doi.org/10.1016/0042-6822\(61\)90332-4](https://doi.org/10.1016/0042-6822(61)90332-4).
- Pfaller CK, Radeke MJ, Cattaneo R, Samuel CE. 2014. Measles virus C protein impairs production of defective copyback double-stranded viral RNA and activation of protein kinase R. *J Virol* 88:456–468. <https://doi.org/10.1128/JVI.02572-13>.
- Ma D, George CX, Nomburg JL, Pfaller CK, Cattaneo R, Samuel CE. 2017. Upon infection, cellular WD repeat-containing protein 5 (WDR5) localizes to cytoplasmic inclusion bodies and enhances measles virus replication. *J Virol* 92:e01726-17. <https://doi.org/10.1128/JVI.01726-17>.
- Nakai M, Imagawa DT. 1969. Electron microscopy of measles virus replication. *J Virol* 3:187–197.
- Nakatsu Y, Ma X, Seki F, Suzuki T, Iwasaki M, Yanagi Y, Komase K, Takeda M. 2013. Intracellular transport of the measles virus ribonucleoprotein complex is mediated by Rab11A-positive recycling endosomes and drives virus release from the apical membrane of polarized epithelial cells. *J Virol* 87:4683–4693. <https://doi.org/10.1128/JVI.02189-12>.
- Katoh H, Kubota T, Kita S, Nakatsu Y, Aoki N, Mori Y, Maenaka K, Takeda M, Kidokoro M. 2015. Heat shock protein 70 regulates degradation of the mumps virus phosphoprotein via the ubiquitin-proteasome pathway. *J Virol* 89:3188–3199. <https://doi.org/10.1128/JVI.03343-14>.
- Ringel M, Heiner A, Behner L, Halwe S, Sauerhering L, Becker N, Dietzel E, Sawatsky B, Kolesnikova L, Maisner A. 2019. Nipah virus induces two inclusion body populations: identification of novel inclusions at the plasma membrane. *PLoS Pathog* 15:e1007733. <https://doi.org/10.1371/journal.ppat.1007733>.
- Zhang S, Jiang Y, Cheng Q, Zhong Y, Qin Y, Chen M. 2017. Inclusion body fusion of human parainfluenza virus type 3 regulated by acetylated α -tubulin enhances viral replication. *J Virol* 91:e01802-16. <https://doi.org/10.1128/JVI.01802-16>.
- Carlos T, Young DF, Schneider M, Simas J, Randall RE. 2009. Parainfluenza virus 5 genomes are located in viral cytoplasmic bodies whilst the virus dismantles the interferon-induced antiviral state of cells. *J Gen Virol* 90:2147. <https://doi.org/10.1099/vir.0.012047-0>.
- Lindquist ME, Lifland AW, Utley TJ, Santangelo PJ, Crowe JE. 2010. Respiratory syncytial virus induces host RNA stress granules to facilitate viral replication. *J Virol* 84:12274–12284. <https://doi.org/10.1128/JVI.00260-10>.
- Cifuentes-Muñoz N, Brantje J, Slaughter KB, Dutch RE. 2017. Human metapneumovirus induces formation of inclusion bodies for efficient genome replication and transcription. *J Virol* 91:e01282-17. <https://doi.org/10.1128/JVI.01282-17>.
- Lahaye X, Vidy A, Pomier C, Obiang L, Harper F, Gaudin Y, Blondel D. 2009. Functional characterization of Negri bodies (NBs) in rabies virus-infected cells: evidence that NBs are sites of viral transcription and replication. *J Virol* 83:7948–7958. <https://doi.org/10.1128/JVI.00554-09>.
- Heinrich BS, Cureton DK, Rahmeh AA, Whelan SP. 2010. Protein expression redirects vesicular stomatitis virus RNA synthesis to cytoplasmic inclusions. *PLoS Pathog* 6:e1000958. <https://doi.org/10.1371/journal.ppat.1000958>.
- Hoenen T, Shabman RS, Groseth A, Herwig A, Weber M, Schudt G, Dolnik O, Basler CF, Becker S, Feldmann H. 2012. Inclusion bodies are a site of ebolavirus replication. *J Virol* 86:11779–11788. <https://doi.org/10.1128/JVI.01525-12>.
- Zhang X, Bourhis J-M, Longhi S, Carsillo T, Buccellato M, Morin B, Canard B, Oglesbee M. 2005. Hsp72 recognizes a P binding motif in the measles virus N protein C-terminus. *Virology* 337:162–174. <https://doi.org/10.1016/j.virol.2005.03.035>.
- Fricke J, Koo LY, Brown CR, Collins PL. 2013. p38 and OGT sequestration into viral inclusion bodies in cells infected with human respiratory syncytial virus suppresses MK2 activities and stress granule assembly. *J Virol* 87:1333–1347. <https://doi.org/10.1128/JVI.02263-12>.
- Koga R, Sugita Y, Noda T, Yanagi Y, Ohno S. 2015. Actin-modulating protein cofilin is involved in the formation of measles virus ribonucleoprotein complex at the perinuclear region. *J Virol* 89:10524–10531. <https://doi.org/10.1128/JVI.01819-15>.
- Nikolic J, Le Bars R, Lama Z, Scrima N, Lagaudrière-Gesbert C, Gaudin Y, Blondel D. 2017. Negri bodies are viral factories with properties of liquid organelles. *Nat Commun* 8:58. <https://doi.org/10.1038/s41467-017-00102-9>.
- Heinrich BS, Maliga Z, Stein DA, Hyman AA, Whelan SP. 2018. Phase transitions drive the formation of vesicular stomatitis virus replication compartments. *mBio* 9:e02290-17. <https://doi.org/10.1128/mBio.02290-17>.
- Courchaine EM, Lu A, Neugebauer KM. 2016. Droplet organelles? *EMBO J* 35:1603–1612. <https://doi.org/10.15252/embj.201593517>.

34. Banani SF, Lee HO, Hyman AA, Rosen MK. 2017. Biomolecular condensates: organizers of cellular biochemistry. *Nat Rev Mol Cell Biol* 18:285. <https://doi.org/10.1038/nrm.2017.7>.
35. Shin Y, Brangwynne CP. 2017. Liquid phase condensation in cell physiology and disease. *Science* 357:eaa4382. <https://doi.org/10.1126/science.aaf4382>.
36. Boeynaems S, Alberti S, Fawzi NL, Mittag T, Polymenidou M, Rousseau F, Schymkowitz J, Shorter J, Wolozin B, Van Den Bosch L, Tompa P, Fuxreiter M. 2018. Protein phase separation: a new phase in cell biology. *Trends Cell Biol* 28:420–435. <https://doi.org/10.1016/j.tcb.2018.02.004>.
37. Alberti S, Gladfelter A, Mittag T. 2019. Considerations and challenges in studying liquid-liquid phase separation and biomolecular condensates. *Cell* 176:419–434. <https://doi.org/10.1016/j.cell.2018.12.035>.
38. Derdowski A, Peters TR, Glover N, Qian R, Utley TJ, Burnett A, Williams JV, Spearman P, Crowe JE. 2008. Human metapneumovirus nucleoprotein and phosphoprotein interact and provide the minimal requirements for inclusion body formation. *J Gen Virol* 89:2698. <https://doi.org/10.1099/vir.0.2008/004051-0>.
39. Gutsche I, Desfosses A, Effantin G, Ling WL, Haupt M, Ruigrok RW, Sachse C, Schoehn G. 2015. Near-atomic cryo-EM structure of the helical measles virus nucleocapsid. *Science* 348:704–707. <https://doi.org/10.1126/science.aaa5137>.
40. Huber M, Cattaneo R, Spielhofer P, Örvell C, Norrby E, Messerli M, Perriard J-C, Billeter MA. 1991. Measles virus phosphoprotein retains the nucleocapsid protein in the cytoplasm. *Virology* 185:299–308. [https://doi.org/10.1016/0042-6822\(91\)90777-9](https://doi.org/10.1016/0042-6822(91)90777-9).
41. Harty RN, Palese P. 1995. Measles virus phosphoprotein (P) requires the NH₂- and COOH-terminal domains for interactions with the nucleoprotein (N) but only the COOH terminus for interactions with itself. *J Gen Virol* 76:2863–2867. <https://doi.org/10.1099/0022-1317-76-11-2863>.
42. Guryanov SG, Liljeroos L, Kasaragod P, Kajander T, Butcher SJ. 2016. Crystal structure of the measles virus nucleoprotein core in complex with an N-terminal region of phosphoprotein. *J Virol* 90:2849–2857. <https://doi.org/10.1128/JVI.02865-15>.
43. Shin Y, Berry J, Pannucci N, Haataja MP, Toettcher JE, Brangwynne CP. 2017. Spatiotemporal control of intracellular phase transitions using light-activated optoDroplets. *Cell* 168:159–171.e14. <https://doi.org/10.1016/j.cell.2016.11.054>.
44. Johansson K, Bourhis J-M, Campanacci V, Cambillau C, Canard B, Longhi S. 2003. Crystal structure of the measles virus phosphoprotein domain responsible for the induced folding of the C-terminal domain of the nucleoprotein. *J Biol Chem* 278:44567–44573. <https://doi.org/10.1074/jbc.M308745200>.
45. Shu Y, Habchi J, Costanzo S, Padilla A, Brunel J, Gerlier D, Oglesbee M, Longhi S. 2012. Plasticity in structural and functional interactions between the phosphoprotein and nucleoprotein of measles virus. *J Biol Chem* 287:11951–11967. <https://doi.org/10.1074/jbc.M111.333088>.
46. Krumm SA, Takeda M, Plemper RK. 2013. The measles virus nucleocapsid protein tail domain is dispensable for viral polymerase recruitment and activity. *J Biol Chem* 288:29943–29953. <https://doi.org/10.1074/jbc.M113.503862>.
47. Das T, Schuster A, Schneider-Schaulies S, Banerjee AK. 1995. Involvement of cellular casein kinase II in the phosphorylation of measles virus P protein: identification of phosphorylation sites. *Virology* 211:218–226. <https://doi.org/10.1006/viro.1995.1394>.
48. Sugai A, Sato H, Yoneda M, Kai C. 2012. Phosphorylation of measles virus phosphoprotein at S86 and/or S151 downregulates viral transcriptional activity. *FEBS Lett* 586:3900–3907. <https://doi.org/10.1016/j.febslet.2012.09.021>.
49. Steinman JB, Kapoor TM. 2019. Using chemical inhibitors to probe AAA protein conformational dynamics and cellular functions. *Curr Opin Chem Biol* 50:45–54. <https://doi.org/10.1016/j.cbpa.2019.02.019>.
50. Höing S, Yeh T-Y, Baumann M, Martinez NE, Habenberger P, Kremer L, Drexler HCA, Küchler P, Reinhardt P, Choidas A, Zischinsky M-L, Zischinsky G, Nandini S, Ledray AP, Ketcham SA, Reinhardt L, Abo-Rady M, Glatza M, King SJ, Nussbaumer P, Ziegler S, Klebl B, Schroer TA, Schöler HR, Waldmann H, Sternecker J. 2018. Dynarrestin, a novel inhibitor of cytoplasmic dynein. *Cell Chem Biol* 25:357–369.e6. <https://doi.org/10.1016/j.chembiol.2017.12.014>.
51. Gomes E, Shorter J. 2019. The molecular language of membraneless organelles. *J Biol Chem* 294:7115–7127. <https://doi.org/10.1074/jbc.TM118.001192>.
52. Toth AM, Devaux P, Cattaneo R, Samuel CE. 2009. Protein kinase PKR mediates the apoptosis induction and growth restriction phenotypes of C protein-deficient measles virus. *J Virol* 83:961–968. <https://doi.org/10.1128/JVI.01669-08>.
53. Tokuriki N, Oldfield CJ, Uversky VN, Berezovsky IN, Tawfik DS. 2009. Do viral proteins possess unique biophysical features? *Trends Biochem Sci* 34:53–59. <https://doi.org/10.1016/j.tibs.2008.10.009>.
54. Xue B, Blocquel D, Habchi J, Uversky AV, Kurgan L, Uversky VN, Longhi S. 2014. Structural disorder in viral proteins. *Chem Rev* 114:6880–6911. <https://doi.org/10.1021/cr4005692>.
55. Moshe A, Gorovits R. 2012. Virus-induced aggregates in infected cells. *Viruses* 4:2218–2232. <https://doi.org/10.3390/v4102218>.
56. Leyrat C, Gerard FCA, de Almeida Ribeiro E, Jr, Ivanov I, Ruigrok RWH, Jamin M. 2010. Structural disorder in proteins of the rhabdoviridae replication complex. *Protein Pept Lett* 17:979–987. <https://doi.org/10.2174/092986610791498939>.
57. Communie G, Crépin T, Maurin D, Jensen MR, Blackledge M, Ruigrok RW. 2013. Structure of the tetramerization domain of measles virus phosphoprotein. *J Virol* 87:7166–7169. <https://doi.org/10.1128/JVI.00487-13>.
58. Ivanov I, Crépin T, Jamin M, Ruigrok RW. 2010. Structure of the dimerization domain of the rabies virus phosphoprotein. *J Virol* 84:3707–3710. <https://doi.org/10.1128/JVI.02557-09>.
59. Cox RM, Krumm SA, Thakkar VD, Sohn M, Plemper RK. 2017. The structurally disordered paramyxovirus nucleocapsid protein tail domain is a regulator of the mRNA transcription gradient. *Sci Adv* 3:e1602350. <https://doi.org/10.1126/sciadv.1602350>.
60. Thakkar VD, Cox RM, Sawatsky B, da Fontoura Budaszewski R, Sourimant J, Wabbel K, Makhosou N, Greninger AL, von Messling V, Plemper RK. 2018. The unstructured paramyxovirus nucleocapsid protein tail domain modulates viral pathogenesis through regulation of transcriptase activity. *J Virol* 92:e02064-17. <https://doi.org/10.1128/JVI.02064-17>.
61. Lier C, Becker S, Biedenkopf N. 2017. Dynamic phosphorylation of Ebola virus VP30 in NP-induced inclusion bodies. *Virology* 512:39–47. <https://doi.org/10.1016/j.virol.2017.09.006>.
62. Poisson N, Real E, Gaudin Y, Vaney M-C, King S, Jacob Y, Tordo N, Blondel D. 2001. Molecular basis for the interaction between rabies virus phosphoprotein P and the dynein light chain LC8: dissociation of dynein-binding properties and transcriptional functionality of P. *J Gen Virol* 82:2691–2696. <https://doi.org/10.1099/0022-1317-82-11-2691>.
63. Tan GS, Preuss MA, Williams JC, Schnell MJ. 2007. The dynein light chain 8 binding motif of rabies virus phosphoprotein promotes efficient viral transcription. *Proc Natl Acad Sci U S A* 104:7229–7234. <https://doi.org/10.1073/pnas.0701397104>.
64. Jacob Y, Badrane H, Ceccaldi P-E, Tordo N. 2000. Cytoplasmic dynein LC8 interacts with lyssavirus phosphoprotein. *J Virol* 74:10217–10222. <https://doi.org/10.1128/jvi.74.21.10217-10222.2000>.
65. Luthra P, Jordan DS, Leung DW, Amarasinghe GK, Basler CF. 2015. Ebola virus VP35 interaction with dynein LC8 regulates viral RNA synthesis. *J Virol* 89:5148–5153. <https://doi.org/10.1128/JVI.03652-14>.
66. Muresan V, Muresan Z. 2012. Unconventional functions of microtubule motors. *Arch Biochem Biophys* 520:17–29. <https://doi.org/10.1016/j.abb.2011.12.029>.
67. Samuel CE. 2001. Antiviral actions of interferons. *Clin Microbiol Rev* 14:778–809. <https://doi.org/10.1128/CMR.14.4.778-809.2001>.
68. Pfaller CK, Mastorakos GM, Matchett WE, Ma X, Samuel CE, Cattaneo R. 2015. Measles virus defective interfering RNAs are generated frequently and early in the absence of C protein and can be destabilized by adenosine deaminase acting on RNA-1-like hypermutations. *J Virol* 89:7735–7747. <https://doi.org/10.1128/JVI.01017-15>.
69. Pfaller CK, Cattaneo R, Schnell MJ. 2015. Reverse genetics of Mononegavirales: how they work, new vaccines, and new cancer therapeutics. *Virology* 479-480:331–344. <https://doi.org/10.1016/j.virol.2015.01.029>.
70. Radecke F, Spielhofer P, Schneider H, Kaelin K, Huber M, Dötsch C, Christiansen G, Billeter MA. 1995. Rescue of measles viruses from cloned DNA. *EMBO J* 14:5773–5784. <https://doi.org/10.1002/j.1460-2075.1995.tb00266.x>.
71. Bailey JK, Fields AT, Cheng K, Lee A, Wagenaar E, Lagrois R, Schmidt B, Xia B, Ma D. 2015. WD repeat-containing protein 5 (WDR5) localizes to the midbody and regulates abscission. *J Biol Chem* 290:8987–9001. <https://doi.org/10.1074/jbc.M114.623611>.
72. Donohue RC, Pfaller CK, Cattaneo R. 2019. Cyclical adaptation of measles virus quasispecies to epithelial and lymphocytic cells: to V, or not to V. *PLoS Pathog* 15:e1007605. <https://doi.org/10.1371/journal.ppat.1007605>.